Scalewise Return to Isotropy in Stratified Boundary Layer Flows

A. Ayet, G. Katul, A. Bragg, J. Redelsperger

HAL Id: hal-02975902

https://hal.univ-brest.fr/hal-02975902v1

Submitted on 8 Oct 2021

Correspondence to:
A. Ayet,
alex.ayet@normalesup.org

Scalewise Return to Isotropy in Stratified Boundary Layer Flows

A. Ayet[1,2] , **G. G. Katul[3]** , **A. D. Bragg[4]** , and **J. L. Redelsperger[1]**

[1]Ifremer, CNRS, IRD, Univ. Brest/ Laboratoire d'Océanographie Physique et Spatiale (LOPS), IUEM, Brest, France, [2]LMD/IPSL, ENS, PSL Université, École Polytechnique, Institut Polytechnique de Paris, Sorbonne Université, CNRS, Paris, France, [3]Nicholas School of the Environment, Duke University, Durham, NC, USA, [4]Department of Civil and Environmental Engineering, Duke University, Durham, NC, USA

Abstract Anisotropic turbulence is ubiquitous in atmospheric and oceanic boundary layers due to differences in energy injection mechanisms. Unlike mechanical production that injects energy in the streamwise velocity component, buoyancy affects only the vertical velocity component. This anisotropy in energy sources, quantified by the flux Richardson number Ri_f, is compensated by a "return to isotropy" (RTI) tendency of turbulent flows. Describing RTI in Reynolds-averaged models and across scales continues to be a challenge in stratified turbulent flows. Using phenomenological models for spectral energy transfers, the necessary conditions for which the widely-used Rotta model captures RTI across various Ri_f and eddy sizes are discussed for the first time. This work unravels adjustments to the Rotta constant, with Ri_f and scale, necessary to obtain consistency between RTI models and the measured properties of the atmospheric surface layer for planar-homogeneous and stationary flows in the absence of subsidence. A range of Ri_f and eddy sizes where the usage of a conventional Rotta model is prohibited is also found. Those adjustments lay the groundwork for new closure schemes.

Plain Language Summary In the atmosphere and in oceans, turbulence dominates much of the exchanges of momentum, heat, water vapor, and scalars such as carbon dioxide, ozone, or methane. Representing turbulence in numerical models of the Earth and climate system remains a first-order problem, requiring the development of simplified approaches to describe the energetics of the flow. One such representation is based on the universal tendency of all turbulent flows to attain an isotropic state, where kinetic energy is equi-partitioned among its three velocity components, labeled "return to isotropy." However, the presence of buoyancy forces and mechanical generation of turbulence causes the flow to be anisotropic at a wide range of eddy sizes. To what degree this additional layer of complexity invalidates the use of existing models based on the aforementioned universal attainment of an isotropic state is explored here. Common representation of such phenomenon within existing climate- and meso-scale models are shown to be satisfactory only for a restricted range of density stratification. The analysis unfolds conditions where adjustments to existing representations are required and others where their use is prohibited. Novel physical processes are also unfolded, providing guidance toward improved turbulence representation in a plethora of models.

1. Introduction

The significance of boundary layer turbulence in the ocean and the atmosphere is not in dispute given its control on a plethora of processes related to the exchange of momentum, heat, and scalars. The description of key flow properties, however, remains a formidable task due to the need of closing the Reynolds-averaged Navier-Stokes equations using appropriate physical models (Canuto et al., 2001; Cuxart et al., 2000; Mellor & Yamada, 1982). Among the minimal ingredients characterizing turbulence are the sources and sinks of turbulent kinetic energy (TKE): shear and buoyancy. Shear production (P_m) impacts the streamwise turbulent velocity component (of variance σ_u^2) whereas buoyancy production/destruction (B) impacts the vertical turbulent velocity component (of variance σ_w^2). A dimensionless quantity used to measure the relative strength of these two energy injection mechanisms is the flux Richardson number $Ri_f = -B/P_m$. The differences in energy injection mechanisms introduce anisotropies in the component-wise turbulent velocity fluctuations (Lane & Sharman, 2014; Lovejoy et al., 2007), with $\sigma_u^2/\sigma_w^2 > 3$ across a wide range of Ri_f (Kaimal & Finnigan, 1994; Sorbjan, 1989).

Despite being anisotropic, turbulence exhibits a universal tendency to relax to an isotropic state where TKE is equally partitioned among its three velocity components. This universal tendency of turbulence has been used to describe pressure-strain interactions that redistribute energy between the three components and hence partially compensate for the anisotropy caused by energy injection mechanisms. This premise forms the basis of numerous turbulence modeling schemes in use today (Abid & Speziale, 1993; Canuto et al., 2001; Cuxart et al., 2000; Drobinski et al., 2007; Launder et al., 1975; Lumley & Newman, 1977; Mellor & Yamada, 1982), especially within meso-scale models such as the Weather Research and Forecasting (or WRF) system. The common closure scheme in use is the Rotta model (Rotta, 1951) that assumes that the magnitude of the energy redistribution among velocity components is directly proportional to the degree of energy anisotropy, which defines the so-called Rotta constant. This scheme continues to draw research attention in the engineering and geophysical fluid dynamics communities alike (Bou-Zeid et al., 2018) since the modeling of the pressure-strain term is key for turbulent closure schemes used in both atmospheric and oceanic models.

A less-studied aspect of this universal tendency of turbulence is the connection between anisotropies appearing in the component-wise turbulent energy spectra at large scales and the attainment of local isotropy at inertial to small scales (Brugger et al., 2018). The "state of the science" to operationally describe such redistribution of energy between differing velocity components at a given scale remains a spectral version of a linear return to isotropy scheme put forth by Rotta (Besnard et al., 1996; Katul et al., 2013). Such a scheme rectifies the absence of a local balance between production and nonlinear transfer across scales for a given velocity component (since the action of viscous dissipation of kinetic energy is small at large scales). It provides a redistribution mechanism of kinetic energy between the three different components at a given scale, assuming a scale-dependent relaxation time scale is set. What is to be explored is whether such a Rotta scheme suffices to capture the main redistribution terms across scales when canonical spectra measured in the atmospheric surface layer (ASL) are used across various Ri_f. To guide this inquiry, we ask what is the Rotta constant associated with the scale-by-scale energy redistribution. Is it dependent on Ri_f and scale? Are there "signatures" of more complex processes such as rapid distortion effects across scales that are amplified or dampened with changes in Ri_f?

In section 2, this question is first addressed from a bulk perspective (i.e., integrated over all scales), extending the results presented in Bou-Zeid et al. (2018) that did not focus on the Rotta constant. Section 3 introduces a spectral model of maximum simplicity (following Katul et al., 2013). The model makes use of a stability-dependent spectral budget for the vertical velocity energy and TKE spectra. The terms in these budgets are then determined for idealized canonical spectral shapes reported for the ASL in the literature for modest deviations in $Ri_f \in [-1.2, +0.1]$ from its neutral value ($=0$). The implications for a "scale-by-scale" Rotta constant are then discussed in section 4. Conclusions are drawn in section 5.

2. A Bulk Analysis

A bulk analysis of the return-to-isotropy problem is first presented so as to introduce notations, concepts, and review the linear Rotta closure scheme. The three instantaneous turbulent velocity components are u', v', and w' in the streamwise (x), cross-stream (y), and vertical (z) directions, respectively, with zero time (or ensemble) averages (i.e., $\overline{u'} = \overline{v'} = \overline{w'} = 0$). Similarly, ρ' is the turbulent density fluctuation around a mean density $\overline{\rho}$. As a logical starting point, a stationary and planar-homogeneous flow at high Reynolds number in the absence of subsidence is considered. The mean velocity in the streamwise direction is denoted by U. Because the focus is on surface layer turbulence, the Coriolis term is ignored. For these idealized flow conditions, the budget equations for the vertical velocity variance $\sigma_w^2 = \overline{w'w'}$ and TKE $e = (1/2)(\overline{u'u'} + \overline{v'v'} + \overline{w'w'})$ reduce to

$$\frac{1}{2}\frac{\partial \sigma_w^2}{\partial t} = 0 = B + R_w - \frac{\epsilon}{3}, \tag{1}$$

$$\frac{\partial e}{\partial t} = 0 = P_m + B - \epsilon. \tag{2}$$

Equation 1 is a balance between buoyancy production or destruction $B = -(g/\overline{\rho})\overline{w'\rho'}$ (g is the gravitational acceleration), the pressure-strain correlation source/sink R_w (discussed below), and viscous dissipation
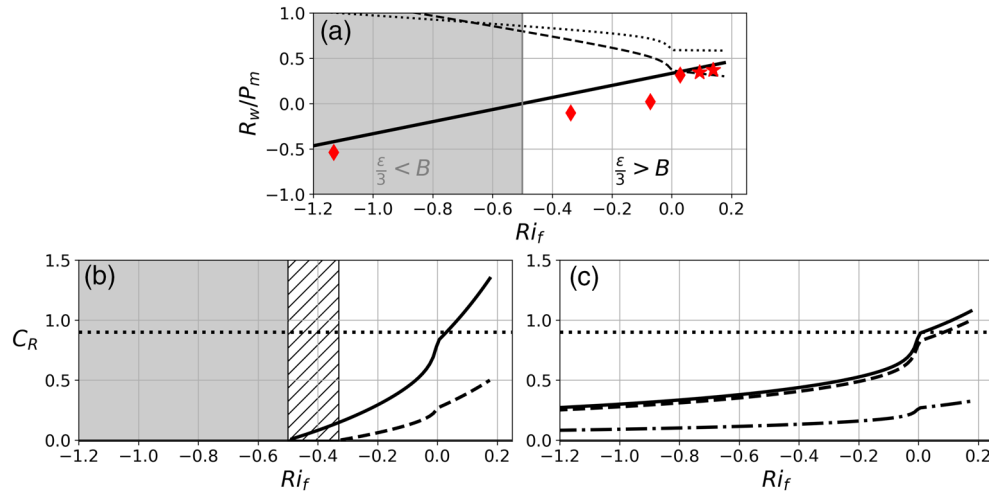
Figure 1. (a) Normalized vertical velocity pressure-strain term R_w/P_m as a function of the flux Richardson number Ri_f. Symbols ★ and ◊ are, respectively, DNS and LES results (from Bou-Zeid et al., 2018). Solid line is from Equation 3. Dashed, dotted lines are Rotta model predictions using a standard Rotta constant C_R=0.9 (Equation 5) without rapid-distortion corrections (dashed) and with rapid distortion corrections (dotted lines). (b) Inferred Rotta constant C_R required for a Rotta model to match the expected pressure-strain dependence (solid line in (a)) as a function of the flux Richardson number Ri_f (Equation 6). Solid and dashed lines are the revised Rotta model without rapid-distortion terms ($\alpha_P = \beta_B = 0$) and with rapid-distortion terms ($\alpha_P = 0.225$ and $\beta_B = 1/3$) respectively. The dotted line is the standard value C_R=0.9 used in canonical boundary layer flows. The shaded region is where no positive C_R value is admitted for the first choice of C_R, α_p, and β_p, and hatches represent the increase of the width of the forbidden region when rapid-distortion terms are included. (c) Same as (b) but for the proposed rapid-distortion coefficients, β_B=2/3 and: α_P=−0.026 (solid line), α_P=0 (dashed line), and α_P=0.225 (dashed-dotted line).

rate ϵ. Equation 2 is a balance between mechanical production $P_m = -\overline{u'w'}(dU/dz)$ (always positive in boundary layer flows), buoyancy production or destruction, and TKE viscous dissipation rate. In both budgets, the turbulent transport of $\overline{w'^2}$ and e is ignored. For near neutral conditions, this assumption may be plausible but becomes questionable for dynamic convective, free convective, and strongly stable conditions as discussed elsewhere (Banerjee et al., 2015; Charuchittipan & Wilson, 2009; Ghannam et al., 2017, 2018; Poggi et al., 2004; Raupach, 1981; Salesky et al., 2013). Data and models for the flux transport terms in the ASL, especially for the vertical velocity skewness, remain in demand. The form of dissipation used here ($\epsilon/3$ in Equation 1) assumes that the total viscous dissipation rate is isotropic. For ASL flows, the isobaric approximation yields $\rho \propto T^{-1}$ where T is potential temperature and thus $B = -(g/\overline{T})\overline{w'T'}$. The pressure-strain term only redistributes energy between the different turbulent velocity components (Pope, 2000) and does not produce or dissipate TKE.

Mechanical production enters the TKE budget whereas buoyancy enters through both the TKE and σ_w^2 budgets. This difference in energy sources (or sinks) results in ASL turbulence being anisotropic, conventionally quantified by the so-called anisotropy tensor (Lumley & Newman, 1977). In the following, the diagonal component of the anisotropy tensor for the vertical direction is used and is given by $r = (\sigma_w^2/e) - 2/3$. It is based on the normalized difference (by $e/2$) between the energy of the vertical turbulent motions, $\sigma_w^2/2$, and the mean TKE, $e/3$. The value r=0 is attained only when energy is equi-partitioned among the velocity components so that $\sigma_u^2 = \sigma_v^2 = \sigma_w^2 = 2e/3$. The term "anisotropy" refers to r unless otherwise stated. Hence, the magnitude and sign of r depends on how far σ_w is from the energy equipartition state. The Rotta model, described below, links the pressure-strain correlation R_w to anisotropy r.

Rearranging Equations 1 and 2 yields an expression for a normalized R_w given by (see Bou-Zeid et al., 2018)

$$\frac{R_w}{P_m} = \frac{2}{3}\left(\frac{1}{2} + Ri_f\right). \tag{3}$$

The normalized R_w only depends on the flux Richardson number $Ri_f = -B/P_m$ and is constant at 1/3 for near-neutral conditions (i.e., Ri_f=0). This relation, shown in Figure 1a (solid line), exhibits similar trends
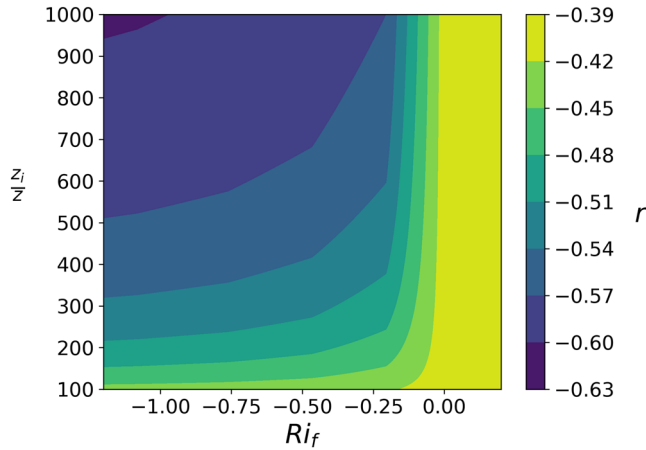
Figure 2. Anisotropy coefficient $r = \sigma_w^2/e - 2/3$ computed from Monin-Obukhov Similarity Theory as a function of the flux Richardson number Ri_f and the ratio between boundary layer height z_i and the measurement height z (see Appendix A for details).

as direct numerical simulations (DNSs) and large eddy simulations (LESs) where the pressure-strain term is computed (stars and diamonds). Figure 1a further shows that R_w should change sign at $Ri_f = -0.5$, that is, be a source (respectively a sink) term in Equation 1 for $Ri_f > -0.5$ (resp. $Ri_f < -0.5$, shaded area), where the buoyancy source B exceeds (resp. is lower than) the dissipation sink $\varepsilon/3$. Any model for the pressure-strain term should thus satisfy this Ri_f dependency for the aforementioned idealized flow conditions in the ASL.

In linear return-to-isotropy models for R_w, anisotropic turbulent flows are assumed to be nudged toward isotropy by the pressure-strain correlation term, which is a source or a sink in the σ_w^2 budget depending on whether $r < 0$ or $r > 0$, respectively. The simplest linear model, the Rotta model, is of the form $R_w \propto (e/\tau)r$ with τ a time scale (Rotta, 1951). In addition to this "slow" component, the Rotta model can be further extended by including rapid-distortion terms (Canuto et al., 2001; Lumley & Khajeh-Nouri, 1975; Pope, 2000). In the case of the vertical velocity component, rapid distortion terms associated with strain and vorticity vanish (Zeman & Tennekes, 1975), and the Rotta model can be written as

$$\frac{R_w}{P_m} = -C_R \frac{(e/\tau)}{P_m}r + \alpha_P + \beta_B Ri_f, \tag{4}$$

where $\tau = e/\varepsilon$ is a model for the relaxation time scale to isotropic state, C_R is the Rotta constant for the slow part, and α_P and β_B are rapid-distortion coefficients associated with the rapid part. Thus, the time scale τ/C_R can be interpreted as the time needed for eddies to redistribute energy among the different components so to attain the equi-partition state where $r = 0$. The constant C_R is positive, and its optimal value for closure modeling is 0.9 (Pope, 2000). This value also has justification for near-neutral flows (Katul et al., 2013) whereas values for α_p and β_p continue to draw research attention. Here, we chose $\alpha_P = 0.225$ and $\beta_B = 1/3$, as derived from renormalization theory and used in the stratified boundary layer model of Canuto et al. (2001).

It is important to stress the differences between Equations 3 and 4. Unlike Equation 4, Equation 3 should be viewed as a constraint on the numerical value of R_w/P_m (under particular assumptions made about the flow such as ignoring the turbulent transport terms), rather than reflecting the underlying dynamics governing R_w/P_m. For example, it would be incorrect to infer from Equation 3 that the physical processes governing R_w are entirely captured by Ri_f, since we know from the Navier-Stokes equation that R_w is dynamically determined by nonlinear processes associated with correlations between the pressure and strain-rate fields of the flow. An analogy can be made to the inertial range of turbulence where the TKE passing through the energy cascade is on average numerically equal to the kinetic energy dissipation rate (under certain flow conditions). This numerical equality, however, simply reflects an energetic balance; the actual dynamical processes governing the energy cascade in the inertial range differ from the dynamical processes governing the energy dissipation rate at the smallest scales of the flow (see Carbone & Bragg, 2020). Similar to this, Equation 3 simply denotes a numerical constraint on the flow (under particular conditions), but the underlying dynamical processes governing R_w/P_m are not reflected in that constraint equation. In contrast, the right-hand side of Equation 4 does represent, in a phenomenological way, the nonlinear dynamical processes governing R_w/P_m, and in particular the energy redistribution time scale τ/C_R.

A large corpus of data in the ASL (e.g., Kader & Yaglom, 1990; Kaimal & Finnigan, 1994; Sorbjan, 1989) show that (i) r depends only on two factors: Ri_f and the relative boundary layer height z_i/z, (ii) for the range of Ri_f investigated in Figure 1a, r is always negative, and (iii) under near neutral conditions, $r \sim -0.4$. This is illustrated in Figure 2, where the ASL measurements of r are presented (the empirical fits can be found in Appendix A). The question we ask below is whether the linear Rotta model, when constrained by those

measurements (i.e. when r is constrained in Equation 4), is compatible with the constraint described by Equation 3. In other words, we evaluate the ability of the linear Rotta model to represent the nonlinear physical processes governing R_w for a flow satisfying the idealized energy balance (1)–(2). As the focus of the present work is on varying stability conditions, the relative boundary layer height is set to 10^3 in the following discussion. Results are not qualitatively sensitive to changes in this height. Note that the properties of anisotropy are valid for planar-homogeneous flow conditions, predominant for the measurements presented in Figure 2. For realistic flow conditions, other factors induce variations in anisotropy (including flux transport terms).

To understand the compatibility between the constraint in Equation 3 and data on r, the TKE budget (2) is inserted into Equation 4 to arrive at a normalized R_w

$$\frac{R_w}{P_m}\bigg|_{Rotta} = C_R(Ri_f - 1)r + \alpha_P + \beta_B Ri_f. \tag{5}$$

For neutral conditions and no rapid-distortion corrections, Equation 5 is compatible with Equation 3 for $C_R \sim 0.9$, that is, the optimal value for closure modeling (Pope, 2000). Figure 1a further shows how this ratio varies with stability for the ASL values of r presented above and a Rotta constant fixed at $C_R = 0.9$. With increasing instability (decreasing Ri_f), the Rotta constant increases, due to r being negative. The Rotta model, both without and with rapid distortion corrections (dashed and dotted lines), is not compatible with the expected values of the pressure-strain term (solid line and symbols) except for $Ri_f \in [0, 0.2]$.

A compatible variation of normalized R_w can be obtained by allowing C_R to adjust with stability. Upon inserting Equations 2 and 4 in (1) yields

$$C_R(Ri_f, z_i/z) = \frac{1}{3r}\left[\frac{1 - 3\alpha_P + (2 - 3\beta_B)Ri_f}{Ri_f - 1}\right], \tag{6}$$

where r is here to be understood as a function of Ri_f and z_i/z (that is, $r = r(Ri_f, z_i/z)$). This equation shows that an "optimal" C_R must be impacted by two parameters: large-scale anisotropy, r (which, in the ASL, depends on Ri_f and z_i/z; see Appendix A), and the flux Richardson number Ri_f, provided that $\alpha_p \neq 1/3$ and $\beta_p \neq 2/3$ simultaneously. The ratio z_i/z can also be interpreted as a relative distance to the wall, hence showing how wall effects in the surface layer impact C_R.

Solid line in Figure 1b shows the optimal Rotta constant without rapid distortion corrections (i.e., $\alpha_P = \beta_B = 0$ in Equation 6). For near-neutral ASL, as mentioned above, $C_R \sim 0.9$, close to the literature-based value. Its value decreases with increasing instability to match the increase of the buoyancy to dissipation ratio, which requires a decreased R_w in Equation 1. This is consistent with an increase of the average size of eddies as instability increases (see, e.g., Katul et al., 2011), implying an increase in their turnover time, and hence in the isotropization time (τ/C_R). For $Ri_f < -0.5$, the sign change of R_w mentioned above implies a negative Rotta constant C_R, which is not physical. These conditions may also be hinting that other sources, and sinks must be considered such as the turbulent flux transport terms. There is thus a range of stability conditions (gray shading) where the linear Rotta model is simply unable to describe R_w for the idealized flow state considered here. Over the range of allowed Ri_f values, the Rotta constant varies by a factor 4 around its value for near-neutral conditions. Inclusion of rapid distortion terms in the Rotta model (dashed line) even decreases the range over which C_R is positive (hatched area).

A negative Rotta constant originate from the sign of the numerator of the last factor of Equation 6, since r and $Ri_f - 1$ are always negative. Setting $\beta_B = 2/3$ and $\alpha_P < 1/3$ is a sufficient (but not necessary) condition for C_R to be positive for all stability conditions. Targeting a $C_R = 0.9$ for neutral conditions with $r \sim 0.4$ and $\beta_B = 2/3$ requires $\alpha_P = -0.026$. The resulting Rotta constant as a function of stability is shown in Figure 1c (full line), along with results with two other values of α_P: $\alpha_P = 0$ (dashed line) and $\alpha_P = 0.225$ (dotted-dashed line, from Canuto et al., 2001). Results show that these new constraints on the rapid distortion terms allow for the Rotta model to be unconditionally valid. However, those values differ from suggested literature-based values when setting $C_R = 0.9$. For β_P, the proposed value is about a factor of 2 higher whereas for α_P, even the sign differs.

Inclusion of vertical turbulent transport terms in the TKE and vertical velocity variance budgets could also decrease the range of stability conditions over which the Rotta constant is negative. Indeed, several studies have shown that the vertical transport of TKE (T_e) is increasingly important for unstable conditions (e.g., Salesky et al., 2013; Wyngaard & Coté, 1971). For the vertical velocity budget, accounting for vertical turbulent transport results in an additional sink term if $T_e > 3T_w$, where T_w is the vertical transport of vertical velocity variance (see Appendix A of Bou-Zeid et al., 2018). This has been used to explain the increase in critical flux Richardson number over roughness sublayers in stably stratified flow, where this condition is met (Freire et al., 2019). In the present situation, the additional sink in the vertical variance budgets can extend the range of stability conditions over which the Rotta model is physical since the condition $B > \varepsilon/3$ will be met for more unstable conditions. Estimates of T_e/T_w are sparse, and both terms are small for near-neutral conditions. We do not discuss this matter quantitatively, but note that including T_e and T_w is expected to increase the range of applicability of the Rotta scheme for a wider range of Ri_f.

The bulk analysis reveals under what conditions a linear Rotta model is compatible with the properties of an idealized ASL flow described by Equations 1 and 2, given ASL measurements of Figure 2. The linear Rotta model (i) should have a Ri_f-dependent Rotta constant and (ii) cannot satisfy mildly unstable ASL anisotropy for the idealized flow conditions considered here when using literature-based rapid-distortion constants. We again stress that these conclusions are valid given the idealized flow conditions considered here, which might not be entirely valid as flow instability increases, and as other terms become important in the TKE and vertical velocity variance budgets. However, maintaining this simplified budget allows performing a scale-by-scale analysis to determine the eddies contributing to the variability in C_R for the restricted range in Ri_f covered here.

3. Spectral Analysis

The R_w analysis and its representation using a Rotta-like closure is now extended scale by scale using a spectral model. The streamwise TKE [$\widetilde{\phi}(k)$] and vertical velocity [$\widetilde{F}_{ww}(k)$] spectra as a function of the streamwise wave number k are considered with normalizing properties $e = \int_0^\infty \widetilde{\phi}(k)dk$ and $\sigma_w^2 = \int_0^\infty \widetilde{F}_{ww}(k)dk$. At very high Reynolds number, a spectral budget for $\widetilde{F}_{ww}(k)$ formulated for eddies in the energy-containing subrange (where anisotropy is large) and inertial subrange (where an isotropic state is approached) is given by Tchen (1953, 1954) and Panchev (1971), as

$$\frac{1}{2}\frac{\partial \widetilde{F}_{ww}(k)}{\partial t} = 0 = \widetilde{B}(k) + \widetilde{R}_w(k) - \widetilde{T}(k). \tag{7}$$

This budget reflects a balance between scalewise buoyancy production/destruction ($\widetilde{B}$, with $\int_0^\infty \widetilde{B}(k)dk = B$), velocity-pressure correlation source/sink ($\widetilde{R}_w$, with $\int_0^\infty \widetilde{R}_w(k)dk = R_w$), and nonlinear transfer of energy across scales ($\widetilde{T}$, with $\int_0^\infty \widetilde{T}(k)dk = 0$), positive over the range of scales considered (i.e., a sink in the above budget). The viscous dissipation term ($\widetilde{\varepsilon} = 2\nu k^2 \widetilde{F}_{ww}(k)$ where ν is the kinematic viscosity) is ignored relative to the transfer term in the production-to-inertial eddy sizes. This assumption is likely to hold at very high Reynolds number when $k\eta << 1$, where $\eta = (\nu^3/\varepsilon)^{1/4}$ is the Kolmogorov microscale (Pope, 2000). Finally, as in the bulk analysis, vertical turbulent flux transport terms are neglected.

Upon integrating Equation 7 over all scales, which requires including $\widetilde{\varepsilon}$ in the budget for small scales (for $k \sim \eta^{-1}$), Equation 1 is recovered (since $\int_0^\infty \widetilde{\varepsilon}(k)dk = \varepsilon$). For the energy-containing and inertial subrange scales considered here, where $\widetilde{\varepsilon}$ is neglected, the nonlinear transfer term $\widetilde{T}$ plays a similar role to the dissipation. The sign of the pressure-strain correlation thus depends on the magnitude of $\widetilde{B}$ relative to $\widetilde{T}$: When the buoyancy term $\widetilde{B}$ exceeds the nonlinear transfer term $\widetilde{T}$ (allowed only for unstable conditions, where $\widetilde{B} > 0$), the pressure-strain correlation should become a sink in the $\widetilde{F}_{ww}$ spectral budget ($\widetilde{R}_w < 0$). We ask now

whether this requirement is compatible with a linear Rotta model for the pressure-strain term in the spectral domain. To answer this question, models for the terms in the spectral budget are required.

3.1. Linear Rotta Model Forced by Idealized ASL Spectra

The state-of-the-science spectral Rotta models (e.g., Besnard et al., 1996; Katul et al., 2013) are conceptually the scale-wise counterparts of the bulk Rotta model (Equation 4). If extended to include rapid-distortion corrections, such spectral Rotta models are given as

$$\widetilde{R}_w(k) = -\frac{\widetilde{C}_R}{\widetilde{\tau}}(k)\left(\widetilde{F}_{ww}(k) - \frac{2}{3}\widetilde{\phi}(k)\right) + \alpha_P \widetilde{P}_m(k) - \beta_B \widetilde{B}(k) \tag{8}$$
$$= -\frac{\widetilde{C}_R}{\widetilde{\tau}}(k)\widetilde{\phi}(k)\widetilde{r} + \alpha_P \widetilde{P}_m(k) - \beta_B \widetilde{B}(k),$$

where $\widetilde{C}_R$ is a (spectral) Rotta coefficient, $\widetilde{r}(k) = \widetilde{F}_{ww}(k)/\widetilde{\phi}(k) - (2/3)$ is the spectral anisotropy, and $\widetilde{\tau}$ is now a scale-dependent turbulence relaxation time scale for which different models have been proposed. To maintain links to prior work (Katul et al., 2013), we selected a $\widetilde{\tau} = \epsilon^{-1/3}k^{-2/3}$ (following Bos et al., 2004). The first rapid distortion correction requires the modeling of a spectral mechanical production $\widetilde{P}_m$ (such that $P_m = \int_0^\infty \widetilde{P}_m(k)dk$). We drop the details about rapid-distortion corrections in the equations within the main text and elaborate on them only in Appendix C and in Figure 5.

Closing the spectral budget requires an analytical expression of spectral anisotropy, which results from choosing idealized expressions for $\widetilde{F}_{ww}$ and $\widetilde{\phi}$ based on measurements. Figures 3a and 3b show measured spectra $\widetilde{\phi}$ and $\widetilde{F}_{ww}$ in an open channel experiment (Katul et al., 2012), over an ice sheet (Cava et al., 2001), grass (Katul et al., 1997), a pine forest (Katul et al., 1999), and a hardwood forest (Katul et al., 1997). Measurements are for near-neutral conditions and for runs where stationary conditions prevailed over extended periods of time.

In agreement with those measurements and earlier work (Banerjee et al., 2015; Grachev et al., 2013; Højstrup, 1982; Kader & Yaglom, 1991; Kaimal, 1978; Kaimal et al., 1972; Katul et al., 2012), only idealized spectral shapes featured in Figure 3c are considered for analytical tractability. These spectra consist of two regimes separated by a transition wave number k_p (vertical line in Figure 3c): (i) the inertial subrange for $k > k_p$, where $\widetilde{\phi}(k) = C_0\epsilon^{2/3}k^{-5/3}$ and $\widetilde{F}_{ww} = C_{ww}\epsilon^{2/3}k^{-5/3}$ (Kolmogorov, 1941), and (ii) the energy-containing range for $k \leq k_p$, where $\widetilde{\phi}(k) = C_0\epsilon^{2/3}k_p^{-2/3}k^{-1}$ and $\widetilde{F}_{ww}(k) = C_{ww}\epsilon^{2/3}k_p^{-5/3}k^0$ (to ensure continuous spectra). The transition wave number is inversely proportional to the measurement height and depends on stability as indicated in Appendix A (Fortuniak & Pawlak, 2015; Kaimal et al., 1972). The spectral constants for boundary layers are taken from Saddoughi and Veeravalli (1994) and are given as $C_0 = (33/55)C_K$ and $C_{ww} = (24/55)C_K$, with $C_K = 1.55$ being the Kolmogorov constant (used for three-dimensional spectra). For highly unstable or stable conditions (not discussed here), these idealized spectral shapes do not hold. However, as long as these shapes exhibit power laws with negative exponents for $k/k_p < 1$, the findings presented below do not qualitatively change (discussed later on).

The resulting turbulent motions are nearly isotropic in the inertial subrange ($\widetilde{r} = 0$ for $k > k_p$) and anisotropic in the energy-containing subrange, with vertical motions having less energy than horizontal motions ($\widetilde{r} < 0$ for $k < k_p$). Returning to Equation 8, this indicates that in the energy-containing range, the Rotta model predicts a source pressure-strain term ($\widetilde{R}_w > 0$). Thus, in the energy-containing range, the ability of the Rotta model to satisfy the spectral budget is conditioned on the relative value of the buoyancy and the nonlinear transfer term, described below. The inertial subrange, where the return-to-isotropy term is almost zero, is not considered.

In the rest of the analysis, the wave number k is normalized by k_p and spectral quantities by powers of ϵ, which leads to an elegant interpretation of the results, independently of variations of k_p and ϵ. Note however that the idealized spectra depend on stability due to the stability-dependence of both k_p (Fortuniak & Pawlak, 2015; Kaimal et al., 1972) and ϵ, which, from Equation 2, can be expressed as $\epsilon = P_m(1 - Ri_f)$.
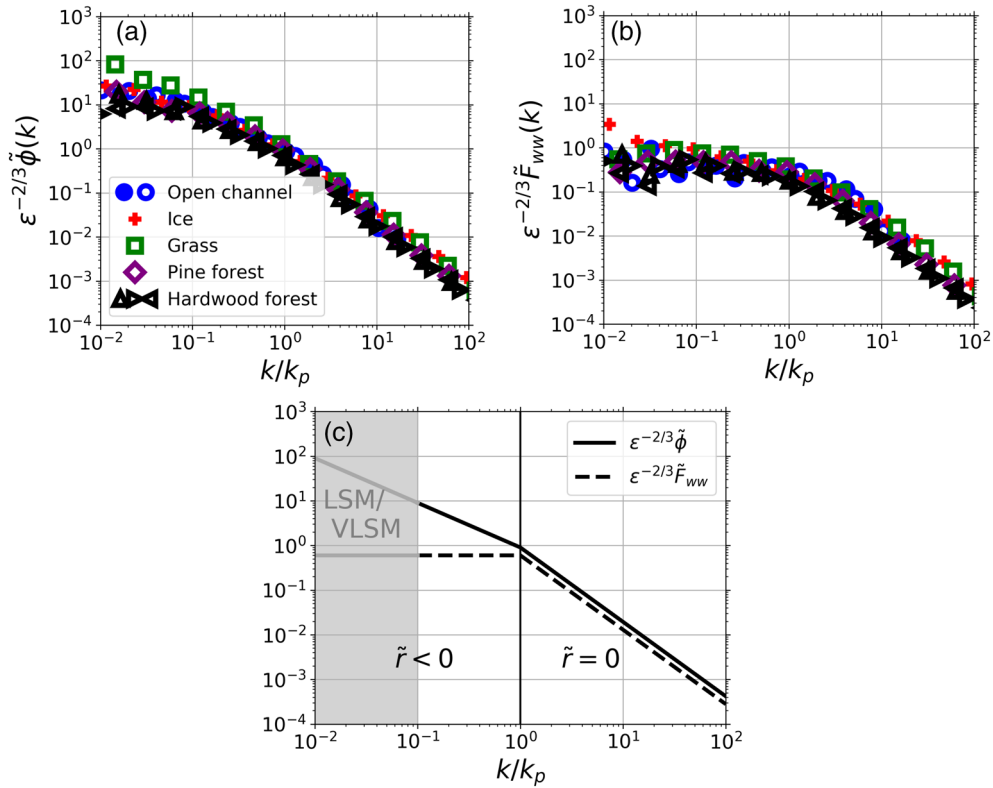
Figure 3. (a, b) Measured streamwise spectra of (a) TKE ($\tilde{\phi}(k)$) (b) vertical velocity ($\tilde{F}_{ww}$) for a near-neutral atmosphere over different terrains, as a function of the relative wave number k/k_p. Spectra have been computed using orthonormal wavelet transforms. (c) Idealized spectra matching measurements, as a function of the relative wave number k/k_p. All spectra are normalized by $\varepsilon^{2/3}$. The vertical line in (c) is the threshold below which $\tilde{F}_{ww}(k)$ is smaller than $(2/3)\tilde{\phi}$. The shaded area in (c) is the range of scales where deviations from single-exponent power laws in the measured spectra are evident, presumably due to eddies associated with large or very large scale motion (LSM and VLSM). The simplified canonical shapes considered here do not include them. Note that, when written in dimensional form, those spectra are stability-dependent due both to variations of ε and k_p with Ri_f.

3.2. Nonlinear and Buoyancy Terms

In the following, a cospectral model for the buoyancy term $\widetilde{B}$ matching several ASL experiments (Katul et al., 2014; Li et al., 2015) is used. It is expressed as a function of the cospectrum of density-velocity fluctuations. For the nonlinear transfer term $\widetilde{T}$, different models have been proposed (e.g., Heisenberg, 1948; Leith, 1967; Obukhov, 1941). In the following, the Heisenberg model (Heisenberg, 1948) is used for illustration to be consistent with prior work (Katul et al., 2012). It represents $\widetilde{T}$ as resulting from the action of the viscosity of small-scale eddies on large-scale eddies and depends on one constant, the Heisenberg constant C_H. Upon choosing the idealized spectra presented above, $\widetilde{B}$ and $\widetilde{T}$ depend only on the flux Richardson number and the relative wave number k/k_p. Details can be found in Appendix B (Equations B2 and B5 for the buoyancy and nonlinear transfer models, respectively), and the resulting normalized spectral budget is shown in Figure 4 (Equation B11).

Figures 4a–4c show the terms in the spectral $\widetilde{F}_{ww}$ budget (Equation 7) as a function of the relative scale for different stability conditions. The buoyancy term $\widetilde{B}$ (dashed line) is a scale-independent sink for stable conditions (Figure 4a) and source for increasing unstable conditions (Figures 4b and 4c). The nonlinear transfer term $\widetilde{T}$ (dashed line) increases with increasing k/k_p in the energy containing range and is independent of stability when normalized and plotted as a function of k/k_p. So is the pressure-strain correlation term $\widetilde{R}_{ww}$ with a Rotta constant $\widetilde{C}_R = 0.9$, which decreases with increasing k/k_p, consistent with a decreasing anisotropy as the isotropic inertial subrange is approached. As mentioned earlier, rapid distortion corrections are not considered here.
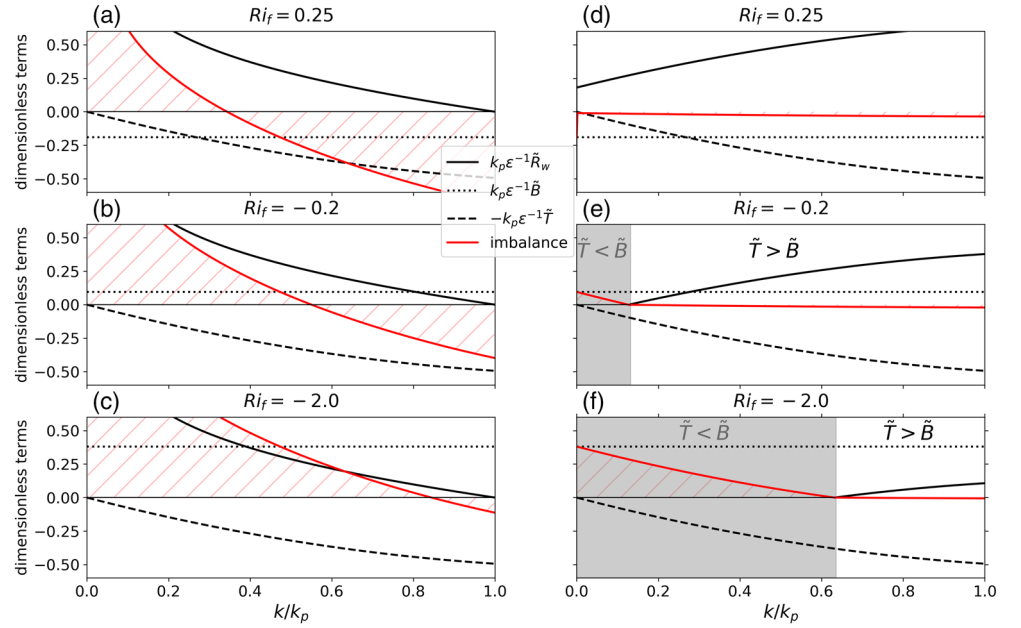
Figure 4. Normalized terms (black) in the spectral budget (7) and residual imbalance (red) as a function of k/k_p for different values of the flux Richardson number Ri_f. In (a)–(c) the Rotta constant in the pressure-strain correlation term is fixed at a constant value of 0.9. In (d)–(f) the Rotta constant evolves with stratification and scale, following Equation 9. The shaded area is where no positive Rotta constant is admitted since the buoyancy source term exceeds the nonlinear transfer sink term. The details of the budget can be found in Appendix B. In this figure, rapid-distortion corrections to the Rotta model are not included ($\alpha_P = \beta_B = 0$).

The imbalance in the $\widetilde{F}_{ww}$ spectral budget cannot be canceled at all scales with such a scale-independent choice of Rotta constant (red line in Figures 4a–4c). The scale-by-scale analysis is now further extended by allowing the Rotta constant to be scale and stratification dependent so as to satisfy the spectral budget.

4. Scale-Dependent Rotta Constant

As with the bulk analysis, we asked the question of whether or not a linear Rotta model is compatible with the spectral budget (7), given the idealized spectral model presented in section 3.1 (based on observations for mildly stable and unstable conditions). As found above, a linear Rotta model cannot satisfy the spectral balance (7) over the entire energy-containing wave number range when $\widetilde{C}_R$ is scale independent. However, it can be satisfied in a limited range of wave numbers if $\widetilde{C}_R$ is allowed to depend on scale and stability. From Equations 7 and 8, and using idealized spectra described in section 3.1, a scale- and stability-dependent Rotta constant needed to maintain the spectral balance can be derived and is given as
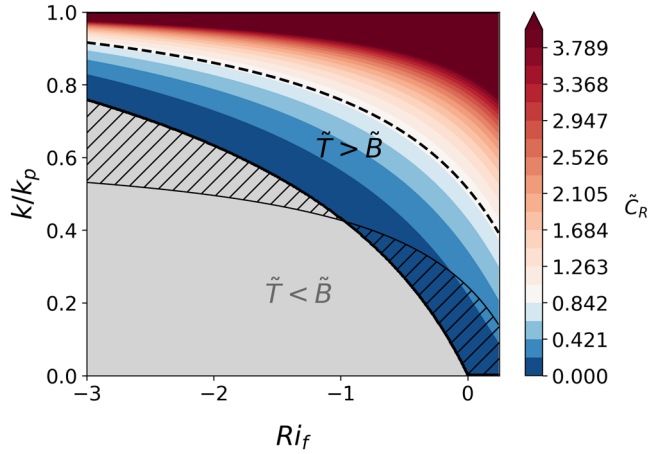
$$\widetilde{C}_R(k/k_p, Ri_f) = \left[\widetilde{r}(k/k_p)\right]^{-1} \left\{ \frac{1 + [\widetilde{\mathscr{A}}_1(k/k_p) - 1]Ri_f}{Ri_f - 1} \right\} \widetilde{\mathscr{A}}_2(k/k_p). \tag{9}$$

Functions $\tilde{A}_1$ and $\tilde{A}_2$ depend on the normalized nonlinear transfer term $k_p \widetilde{T}/\epsilon$ and on the time scale $\tilde{\tau}$. For the Rotta time scale selected here, they are given as

$$\widetilde{\mathscr{A}}_1(k/k_p) = \frac{4}{7}\left[\frac{k_p\widetilde{T}}{\epsilon}(k/k_p)\right]^{-1}, \quad \widetilde{\mathscr{A}}_2(k/k_p) = C_0^{-1}\left(\frac{k}{k_p}\right)^{1/3}\frac{k_p\widetilde{T}}{\epsilon}(k/k_p), \tag{10}$$

where the normalized nonlinear transfer term reads, when modeled with the Heisenberg model,

$$\frac{k_p\widetilde{T}}{\epsilon}(k/k_p) = 2C_H C_0^{1/2} C_{ww}\left[\frac{2}{3}\frac{k}{k_p} - \frac{1}{4}\left(\frac{k}{k_p}\right)^2\right]. \tag{11}$$

Figure 5. Scalewise Rotta constant $\tilde{C}_R$ as a function of the relative wave number $k/k_p < 1$ (in the energy-containing subrange) and the flux Richardson number Ri_f, following Equation 9. Dashed line is the level where $\tilde{C}_R$ matches its standard value of 0.9. The shaded region is where no positive $\tilde{C}_R$ is admitted. The area varies when rapid-distortion terms are included in the Rotta model (hatches), as described in Appendix C.

The Heisenberg constant C_H is set to $(8/9)C_0^{-3/2}$ to recover the TKE spectral properties under neutral conditions (Banerjee & Katul, 2013). Details about the derivation of Equations 9–11 are in Appendix C, which also contains a general expression of $\widetilde{C}_R$ when rapid-distortion terms are included in the spectral Rotta model (Equation C14). Note that, in the above expressions, the scale parameter is implicitly stability-dependent through the stability dependence of k_p.

Figures 4d–4f show the terms of the $\widetilde{F}_{ww}$ spectral balance with the pressure-strain term parametrized by means of a scale- and stability-dependent Rotta constant (Equation 9). For stable stratification (Figure 4d), the balance is satisfied at all scales (the red line is uniformly zero). With increased instability (Figures 4e and 4f), the dynamic $\widetilde{C}_R(k)$ model cannot guarantee a positive Rotta constant at large scales (or small k/k_p) because the redistribution model can no longer predict the sign of the energy exchanges: for scales large enough (shaded area), the buoyancy source term exceeds the nonlinear transfer sink term, and hence, the pressure-strain term is expected to change sign to maintain a scalewise balance. From Equation 8, this implies a negative Rotta constant given that the sign of the anisotropy factor is constant (and negative) in the energy-containing range. The range of scales over which the Rotta constant is negative increases with increasing instability (i.e., for $k/k_p < 0.1$ and $k/k_p < 0.4$ in Figures 4c and 4d, respectively). Similar to the bulk analysis, the spectral model reveals that, for the idealized flow conditions described in Figure 3c (and based on measurements), (i) a scale- and stability-dependent Rotta constant is required to close the spectral budget and that (ii) below a critical wave number, a linear Rotta model fails to predict the correct sign of the pressure-strain correlation term.

The scale-by-scale picture is however more refined. It reveals that for stability conditions over which the bulk Rotta model fails to predict the correct sign of the pressure-strain correlation term (for $Ri_f < -0.5$, see Figure 1b), its spectral counterpart is still valid, but over a limited range of scales. This behavior is summarized in Figure 5, which shows the increase of the region over which Rotta constant is negative as a function of stability and scale (shaded area, where $\widetilde{C}_R < 0$). The figure also reveals that as the scale increases, the range of stability conditions over which the Rotta model is not physical increases. This finding indicates that for larger and more anisotropic eddies, the classical linear Rotta model becomes physically unrealistic.

Accounting for rapid-distortion terms in the Rotta model (as described in Appendix C1) changes the area where the Rotta constant is not physical (hatches in Figure 5). However, unlike the bulk case, the area increases for $k/k_p < 0.4$ and decreases for $k/k_p > 0.4$. This is a consequence of the antagonist behavior of the two rapid-distortion terms, respectively, $\alpha_P \widetilde{P}_m$ and $-\beta_B \widetilde{B}$ (see Equation 8). When the rapid distortion terms are included in the $\widetilde{F}_{ww}$ budget as part of the Rotta model, the first term is an additional source in the budget (since $\widetilde{P}_m$ is a source, as in the bulk model), and the second term acts as an additional sink for unstable conditions (since $\widetilde{B} > 0$ and $\beta_B > 0$). Hence, at a given scale k/k_p, the (negative) threshold Ri_f below which the buoyancy source exceeds the nonlinear transfer sink (and hence the slow Rotta term must change sign) is displaced due to these two additional terms. Whether the threshold Ri_f increases or decreases depends on the relative magnitude of $\alpha_P \widetilde{P}_m$ with respect to $-\beta_B \widetilde{B}$, that is, whether the two additional terms add up as an additional source or a sink in the budget. This further depends on the relative scale k/k_p, since $\widetilde{P}_m$ and $\widetilde{B}$ are both scale dependent. The finding here shows that the spectral behavior of the rapid-distortion terms is nontrivial as compared to the bulk case. Choosing rapid-distortion constants that result in a unconditionally positive Rotta constant (as in the bulk case; Figure 1b), although feasible, is nontrivial and is outside of the scope of the present work. It would require choosing and validating scale-dependent models for α_P and β_B.

Figure 5 also summarizes the variations of the "optimal" Rotta constant as a function of scale and stability, in the region where it is positive. Consistent with the bulk analysis, the Rotta constant decreases with

increasing instability at a fixed large scale. As the inertial subrange is approached ($k/k_p \to 1$), the observed increase in $\widetilde{C}_R$ results from anisotropy decreasing to zero, and hence the expression for the Rotta constant losing physical meaning (i.e., the solution becomes degenerate). However, far enough from this limit (e.g., on the left of the dashed line for which $\widetilde{C}_R = 0.9$), the behavior of $\widetilde{C}_R$ is physically sound. Figure 5 shows that $\widetilde{C}_R$ decreases with increasing scale. This dependence is identical to the nonlinear transfer term variation with k/k_p, which is predicted to decrease down to zero as large scales are approached (dashed lines in Figure 4). It can be traced back to function $\tilde{A}_2$ (Equation 10), proportional to the nonlinear transfer term. From a physical perspective, this link implies that the efficiency of eddies at redistributing energy between the different components (C_R^{-1}) is related to their efficiency at transporting energy toward small scales ($\widetilde{T}$). Choosing other models for the nonlinear transfer term does not alter this finding, but it affects variations of $\widetilde{C}_R$ with k/k_p.

The above analysis relies on turbulence satisfying idealized spectral budgets with a prescribed form of the spectra and their variation with stability (through ϵ and k_p). Those spectra are limited by several factors. At large scales ($k < 10^{-1} k_p$), the measured spectra start deviating from the idealized -1 or 0 power laws (Figures 3a and 3b). For simplicity, this effect is neglected, but its inclusion does not qualitatively change the findings here. In the energy-containing range, the -1 power law of the TKE spectra has been a subject of debate due to differences and uncertainties in the measurements at this range of scales and possible influence of stability and the use of Taylor's frozen turbulence hypothesis (Banerjee et al., 2015; Drobinski et al., 2007; Katul & Chu, 1998; Marusic et al., 2010; Morrison et al., 2002; Nickels et al., 2005; Nikora, 1999). Again, the results here are not significantly dependent on the choice of the power law for $\widetilde{\phi}$ as long as it is smaller than 0. The general expression of $\widetilde{C}_R$ presented in Appendix C is also independent of the choice of the power law. As instability increases, the -1 power law describing the large-scale TKE spectrum begins to migrate toward a $-5/3$ exponent as evidenced by a number of ASL experiments (Banerjee et al., 2015; Kader & Yaglom, 1991). In fact, for strongly unstable (near convective) cases (not considered here), measurements (Kader & Yaglom, 1991) further suggest that the spectra of TKE and w can be almost discontinuous at the transition wave number k_p. These spectra exhibit a $-5/3$ law at large scales with a discontinuity, followed by another $-5/3$ regime associated with Kolmogorov scaling. Hence, in those situations anisotropy $\tilde{r}$ changes sign, with more energy in the vertical than in the horizontal turbulent components. Finally, additional terms could partly explain the inconsistency of the spectral Rotta model revealed by the above analysis. As for the bulk case, inclusion of vertical transport of turbulence in the $\widetilde{F}_{ww}$ spectral budget can act as an additional sink. Given that the bulk transport terms are small for the mildly unstable conditions considered here, inclusion of their effect will not qualitatively change the above analysis, except perhaps above roughness sublayers (Freire et al., 2019).

5. Conclusion

This work analyzed the implications of using linear return-to-isotropy models of the pressure-strain correlation (or simply Rotta models) to describe planar-homogeneous and stationary boundary layer turbulence for mildly stable to mildly unstable conditions. The flow was analyzed by combining TKE and vertical velocity variance budgets representing the bulk and scale-by-scale properties of turbulence. The analysis required estimates of turbulence anisotropy as well as spectral shapes. Those were externally supplied from measurements in the ASL for which a rich literature on both velocity spectral shapes and bulk anisotropy variations, along with their dependence with flow instability, is available. The analysis revealed two inconsistencies when using a linear Rotta model to describe return to isotropy for the idealized flow conditions described by those measurements. The first is that for some stability conditions and eddy sizes, the Rotta model is not physical. It should thus be amended by other processes beyond a linear return to isotropy such as quadratic dependencies on anisotropy. The second is that, to satisfy the two aforementioned budgets outside of the nonphysical range, the Rotta constant should depend on stability and scale. Both results are sensitive to the balance considered. In particular, the relative importance of the vertical flux transport by turbulence terms, which were neglected in the present study, cannot be overlooked for stratified ASL flow conditions. The work here has also remained "silent" on another anisotropy-producing mechanism, which is likely to be of significance in the sublayers below the ASL. This mechanism is labeled "wall-blocking" effect because the presence of an impervious boundary dampens w', which, in turn, is sensed everywhere in the domain by

p', the pressure perturbation. Classical closure theories accommodate this effect as a new term in the Rotta return-to-isotropy scheme (or its spectral version) as discussed elsewhere (McColl et al., 2016). In smooth-wall boundary layers, wall blocking appeared to be minor in the absence of stratification for the log region. However, the interplay between wall blocking and density stratification has not been explicitly considered and remains a research topic better kept for the future.

Appendix A: Anisotropy According to Monin-Obukhov Similarity Functions

In the ASL, stability dependence of bulk flow statistics and spectral properties are routinely analyzed in the context of Monin-Obukhov Similarity Theory (MOST Foken, 2006; Monin & Obukhov, 1954). From dimensional arguments, dimensionless turbulent fluctuations and shear should depend only on a dimensionless stability parameter $\zeta = z/L$ (negative for unstable and positive for stable stratification), where z is the distance from the boundary (or displacement height) and L is the Obukhov length, and on the boundary layer height, z_i.

Numerous ASL measurements (e.g., Sorbjan, 1989, Table 4.2) have provided the following expressions for dimensionless shear

$$\phi_m(\zeta) = \frac{\kappa z}{(-\overline{u'w'})^{1/2}} \frac{dU}{dz} = \begin{cases} 1 + 4.7\zeta & \text{if } \zeta \geq 0 \\ (1 - 15\zeta)^{-1/4} & \text{if } \zeta < 0 \end{cases}, \tag{A1}$$

dimensionless vertical velocity standard deviation

$$\phi_w(\zeta) = \frac{\sigma_w}{(-\overline{u'w'})^{1/2}} = \begin{cases} 1.25 & \text{if } \zeta \geq 0 \\ 1.25(1 - 3\zeta)^{1/3} & \text{if } \zeta < 0 \end{cases}, \tag{A2}$$

and dimensionless horizontal velocity standard deviation

$$\phi_{u_h}\left(\zeta, \frac{z_i}{z}\right) = \left(\frac{\overline{u'_h u'_h}}{-\overline{u'w'}}\right)^{1/2} = \begin{cases} 2.28 & \text{if } \zeta \geq 0 \\ \left[12 - 0.5\frac{z_i}{z}\zeta\right]^{1/3} & \text{if } \zeta < 0 \end{cases}, \tag{A3}$$

where $\kappa = 0.4$ is the von Kármán constant and u_h is either u or v. Finally, the flux Richardson number and the stability parameter are linked through $Ri_f = \zeta/\phi_m(\zeta)$.

Figure 2 shows anisotropy

$$r = \frac{\phi_w^2}{(1/2)(\phi_w^2 + \phi_u^2 + \phi_v^2)} - \frac{2}{3} \tag{A4}$$

computed for the aforementioned dimensionless functions as a function of the flux Richardson number and the relative boundary layer height. For the range of stability conditions investigated in the present work ($Ri_f > -5$), which exclude the free convection limit, Figure 2 shows that the anisotropy ratio is always negative. This indicates that more energy is concentrated in the horizontal than in the vertical turbulent components. In the main text, the boundary layer height is set to be 10^3 times higher than the measurement height. The sign of the anisotropy ratio is not sensitive to the choice of the boundary layer height (not shown).

Finally, as an illustration, we show below an example of a model of k_p from the Kansas experiment (Kaimal & Finnigan, 1994):

$$zk_p^k(\zeta) = \begin{cases} \zeta, & \zeta > 2 \\ 1.1 + 0.45\zeta, & 1 < \zeta \le 2 \\ 0.55 + \zeta, & 0 \le \zeta \le 1 \\ 0.55 + 0.38\zeta, & -1 \le \zeta < 0 \\ 0.17, & \zeta < -1 \end{cases}. \tag{A5}$$

Note however that the results of the main text are all expressed as a function of k/k_p and are hence independent of a particular model of k_p.

Appendix B: Details on the Spectral Budget

At very high Reynolds number, a spectral budget for $\widetilde{F}_{ww}(k)$ formulated for large and inertial subrange eddies follows from Tchen (1953, 1954) and Panchev (1971) and is given by

$$\frac{1}{2} \frac{\partial \widetilde{F}_{ww}(k)}{\partial t} = 0 = \widetilde{B}(k) + \widetilde{R}_w(k) - \widetilde{T}(k). \tag{B1}$$

Details on the different terms of this budget are now provided. The model for the pressure-strain term $\widetilde{R}$ is presented in Equation 8.

For the ASL with an isobaric approximation, the buoyancy source/sink term $\widetilde{B}$ is related to the cospectrum of temperature fluctuations $\widetilde{F}_{wT}$ as

$$\widetilde{B}(k) = -\frac{g}{T}\widetilde{F}_{wT}(k), \tag{B2}$$

where the cospectrum has the normalizing property $\overline{w'T'} = \int_0^\infty \widetilde{F}_{wT}(k)dk$. Katul et al. (2014) and Li et al. (2015) proposed a cospectrum matching both a theoretical spectral budget and ASL measurements, of the form $\widetilde{F}_{wT}(k) = C_{wT}\varepsilon^{1/3}\frac{dT}{dz}k^{-7/3}$ for $k \ge k_p$ and $\widetilde{F}_{wT}(k) = C_{wT}\varepsilon^{1/3}\frac{dT}{dz}k_p^{-7/3}$ for $k \le k_p$. The transition wave number k_p between the energy-containing and the inertial subranges is proportional to the measurement height and changes slightly with stratification (Fortuniak & Pawlak, 2015; Kaimal et al., 1972). The spectral constant reads $C_{wT} = C_{uw}Q(\zeta)$ with

$$Q(\zeta) = 1 - \frac{C_T\zeta}{(1 - C_{1T})C_0(\phi_m - \zeta)}, \tag{B3}$$

$C_0 = 0.9$, $C_T = 0.8$, $C_{1T} = 3/5$ (Katul et al., 2014), and ζ the stability parameter defined in Appendix A.

The nonlinear transfer term $\widetilde{T}$ is represented using the Heisenberg model (Heisenberg, 1948), to be consistent with the models of the buoyancy and Rotta terms (as explained in the main text). Within this spectral approach of turbulence, developed by Heisenberg (1948) and Tchen (1953, 1954) (and summarized in Panchev, 1971, pp. 203–224), what is described is an integrated spectral budget, obtained by integration of Equation B1 over streamwise wave numbers between k and ∞. This results in an equation describing the spectral balance for a particular wavelength k, the lower limit of the integral. What is then modeled is $\widetilde{W}$, the integral of the nonlinear transfer term,

$$\widetilde{W}(k) = \int_k^\infty \widetilde{T}(p)dp, \tag{B4}$$

and hence $\widetilde{T}(k) = -\frac{d}{dk}\widetilde{W}(k)$. Following Heisenberg (1948), $\widetilde{W}$ is modeled as resulting from the action of viscosity generated by eddies of wavelength greater than k on eddies of wavelength smaller than k

$$\widetilde{W}(k) = -2C_H \int_k^\infty \left(\frac{\widetilde{\phi}(p)}{p^3} \right)^{1/2} dp \int_0^k p^2 \widetilde{F}_{ww}(p)dp, \tag{B5}$$

where $C_H = (8/9)C_0^{-3/2}$ for consistency with Kolmogorov scaling in the inertial range (Banerjee & Katul, 2013; Schumann, 1994). Since $\widetilde{W}$ models the nonlinear energy transfer in the vertical component of turbulence, enstrophy (the second factor) is here computed from $\widetilde{F}_{ww}$ (and not from the TKE spectrum $\widetilde{\phi}$ as in Panchev, 1971, where the transfer term was computed for the TKE spectral budget).

Expressions of the terms of the spectral budget in the energy-containing range ($k \leq k_p$) are presented for idealized spectra $\widetilde{\phi}(k)$ and $\widetilde{F}_{ww}(k)$ presented in the main text (and drawn in Figure 3c). First, the nonlinear transfer term reads, from derivation of (B5) with respect to k,

$$\widetilde{T}(k) = 2C_H C_0^{1/2} C_{ww} k_p^{-1} \epsilon \left[\frac{2}{3} \frac{k}{k_p} - \frac{1}{4} \left(\frac{k}{k_p} \right)^2 \right]. \tag{B6}$$

Second, the pressure-strain term following the Rotta model without rapid-distortion corrections (Equation 8, with $\alpha_P = \beta_B = 0$) reads

$$\widetilde{R}_w = -C_0^{1/2} C_R \epsilon k_p^{-1} \left(\frac{k}{k_p} \right)^{2/3} \left[C_{ww} - \frac{2}{3} C_0 \frac{k_p}{k} \right]. \tag{B7}$$

Finally, using the idealized $\widetilde{F}_{wT}$ cospectra presented above, the spectral buoyancy term can be rewritten as a function of the flux Richardson number. This results from the bulk buoyancy B being expressed as a function of (i) the spectral buoyancy term

$$\begin{aligned} B &= -\frac{g}{T} \int_0^\infty \widetilde{F}_{wT}(p)dp \\ &= -\frac{7}{4} \epsilon^{1/3} C_{wT} \frac{g}{T} \frac{dT}{dz} k_p^{-4/3}(k), \quad k \leq k_p, \\ &= \frac{7}{4} k_p \widetilde{B} \end{aligned} \tag{B8}$$

and (ii) TKE dissipation, using the bulk TKE budget (Equation 2)

$$B = \epsilon \frac{Ri_f}{1 - Ri_f}. \tag{B9}$$

This yields

$$\widetilde{B} = \frac{4}{7} \epsilon k_p^{-1} \frac{Ri_f}{Ri_f - 1}, \quad k \leq k_p. \tag{B10}$$

The spectral budget (B1) (or Equation 7) normalized by ϵk_p^{-1} thus reads

$$\frac{4}{7} \frac{Ri_f}{Ri_f - 1} - C_0^{1/2} C_R \left[C_{ww} \frac{k}{k_p} - \frac{2}{3} C_0 \right] - 2C_H C_0^{1/2} C_{ww} \left[\frac{2}{3} \frac{k}{k_p} - \frac{1}{4} \left(\frac{k}{k_p} \right)^2 \right] = 0, \tag{B11}$$

a balance between (from left to right) dimensionless buoyancy, energy redistribution, and nonlinear transfer of energy across scales. The terms have been normalized by ϵk_p^{-1} and are plotted in Figure 4. As already mentioned above, we again stress that, in this budget, rapid-distortion corrections have not been included in the Rotta model of the energy redistribution term.

Appendix C: General Derivation of the Scale- and Stratification-Dependent Rotta Constant

This section presents the steps leading to a generalized form of Equation 9, valid for different choices of time scales and nonlinear transfer models, and including rapid-distortion corrections to the Rotta model.

The spectral Rotta models considered in the literature (Bos et al., 2004; Katul et al., 2013) only contain a slow component. In this work, the spectral Rotta model is generalized by adding rapid distortion terms on the basis of the bulk model of Canuto et al. (2001), such that

$$\widetilde{R}_w = -\frac{\widetilde{C}_R}{\widetilde{\tau}}\left(\widetilde{F}_{ww} - \frac{2}{3}\widetilde{\phi}\right) + \alpha_P \widetilde{P}_m - \beta_B \widetilde{B}, \tag{C1}$$

where α_P and β_B are set to their bulk values of 0.225 and 0.35, respectively.

The scalewise production term $\widetilde{P}_m$ is obtained from a spectral balance for TKE (e.g., Tchen, 1953), which for stationary and planar-homogeneous flow at high Reynolds number in the absence of subsidence reads

$$\frac{\partial \widetilde{\phi}}{\partial t} = 0 = \widetilde{P}_m + \widetilde{B} - \widetilde{T}_\phi. \tag{C2}$$

Hence, the nonlinear Rotta scheme model reads

$$\widetilde{R}_w = -\frac{\widetilde{C}_R}{\widetilde{\tau}}\left(\widetilde{F}_{ww} - \frac{2}{3}\widetilde{\phi}\right) + \alpha_P(\widetilde{T}_\phi - \widetilde{B}) - \beta_B \widetilde{B}. \tag{C3}$$

The nonlinear transfer term $\widetilde{T}_\phi$ is computed using a Heisenberg viscosity approach (see Appendix B for its application to the vertical velocity spectral budget; Heisenberg, 1948). Heisenberg (1948) and Tchen (1953,1954) model the terms of an integrated spectral budget, derived by integrating Equation C2 between k and ∞. The nonlinear transfer term in the resulting equation

$$\widetilde{W}_\phi(k) = \int_k^\infty \widetilde{T}_\phi(p)dp \tag{C4}$$

is then modeled as resulting from the action of viscosity of eddies of wavelength greater than k on eddies of wavelength smaller than k, that is,

$$\tilde{W}_\phi(k) = -2C_H \int_k^\infty \frac{\tilde{\phi}(p)^{1/2}}{p^3} dp \int_0^k p^2 \tilde{\phi}(p)dp, \tag{C5}$$

where $C_H = (8/9)C_0^{-3/2}$. The idealized TKE spectrum presented in Figure 3 yields the following form of the nonlinear transfer term $\widetilde{T}_\phi(k) = -\frac{d}{dk}\widetilde{W}_\phi(k)$ for $k \leq k_p$,

$$\widetilde{T}_\phi(k, \eta) = 2C_H C_0^{3/2}\left[\frac{2}{4} - \frac{1}{4}\frac{k}{k_p}\right]\epsilon k_p^{-1}. \tag{C6}$$

The time scale $\widetilde{\tau}$ is usually assumed to be k dependent and to depend only on inertial range variables (ϵ, conserved across the cascade, k and k_p) in conventional spectral models (e.g., Besnard et al., 1996; Katul et al., 2013; Panchev, 1971). From dimensional considerations, its general form in the energy-containing range ($k \leq k_p$) is

$$\widetilde{\tau}(k) \propto \epsilon^{-1/3}k_p^{-2/3}\left(\frac{k}{k_p}\right)^m = \widetilde{\phi}(k)\mathscr{A}_\tau \epsilon^{-1} k_p \left(\frac{k}{k_p}\right)^{m-a} \tag{C7}$$

with $\widetilde{\phi}(k) = C_0\epsilon^{2/3}k_p^{-5/3-a}k^a$ the TKE spectrum of slope a, C_0 is the Kolmogorov constant, and m and $\mathscr{A}_\tau$ depend on the model used for the time scale. For a TKE spectrum with $a = -1$, the time scale $\widetilde{\tau} = \epsilon^{-1/3}$

$k^{-2/3}$ (used in the following Bos et al., 2004; Katul et al., 2013) corresponds to $m=-2/3$ and $A_\tau = C_0^{-1}$, while other estimates of the time scale, for example, $\widetilde{\tau} = k^{-3/2}\widetilde{\phi}^{-1/2}$ (Besnard et al., 1996), correspond to $m=-1$ and $A_\tau = C_0^{-3/2}$.

Using the Rotta model (C3) and the time scale (C7), the $\widetilde{F}_{ww}$ spectral budget can be solved for $\widetilde{C}_R$, yielding

$$\widetilde{C}_R = \widetilde{r}^{-1}\left\{-1 + [(1-\beta_B)-\alpha_P]\frac{\widetilde{B}}{\widetilde{T}} + \alpha_P\frac{\widetilde{T}_\phi}{\widetilde{T}}\right\}\frac{\widetilde{T}}{\epsilon}\mathscr{A}_\tau k_p^{1-m+a}k^{m-a}. \tag{C8}$$

Evaluation of Equation C8 requires an expression for the ratio $\widetilde{B}/\widetilde{T}$. We now show that, regardless of the choosen model for the nonlinear transfer of energy across scales ($\widetilde{T}$), this ratio reads

$$\frac{\widetilde{B}}{\widetilde{T}} = \widetilde{\mathscr{A}}_1\frac{Ri_f}{Ri_f - 1}. \tag{C9}$$

The constant $\widetilde{\mathscr{A}}_1$ depends on the model and is given below. Different models for the nonlinear transfer term (Heisenberg, 1948; Leith, 1967; Obukhov, 1941) all assume that it depends on the TKE spectrum and hence should depend only on k, k_p, and ϵ. Dimensional considerations then yield that

$$\widetilde{T} = \widetilde{\mathscr{B}}_{NL}\epsilon k_p^{-1}, \tag{C10}$$

where $\widetilde{\mathscr{B}}_{NL}$ depends only on k/k_p. For the Heisenberg (1948) model (Equation B6), used in the following, it reads

$$\widetilde{\mathscr{B}}_{NL} = 2C_H C_0^{1/2}C_{ww}\left[\frac{2}{3}\frac{k}{k_p} - \frac{1}{4}\left(\frac{k}{k_p}\right)^2\right]. \tag{C11}$$

In the general case, dividing the expression of the buoyancy term derived in Appendix B (Equation B10)

$$\widetilde{B} = \frac{4}{7}\epsilon k_p^{-1}\frac{Ri_f}{Ri_f - 1}, \quad k \leq k_p, \tag{C12}$$

by Equation C10, yields Equation C9 with

$$\widetilde{\mathscr{A}}_1 = \frac{4}{7}\epsilon\widetilde{T}^{-1}k_p^{-1} = \frac{4}{7}\widetilde{\mathscr{B}}_{NL}^{-1}. \tag{C13}$$

By using (C9) in Equation C8, we obtain the generalized expression of the Rotta constant

$$\widetilde{C}_R = \widetilde{r}^{-1}\left\{\frac{1 + [(1-\beta_B - \alpha_P)\widetilde{\mathscr{A}}_1 - 1]Ri_f}{Ri_f - 1} + \alpha_P\frac{\widetilde{T}_\phi}{\widetilde{T}}\right\}\widetilde{\mathscr{A}}_2, \tag{C14}$$

where, using (C13),

$$\tilde{A}_2 = \mathscr{A}_\tau k_p^{1-m+a}k^{m-a}\frac{\widetilde{T}}{\epsilon} = \mathscr{A}_\tau k_p^{-m+a}k^{m-a}\widetilde{\mathscr{B}}_{NL}. \tag{C15}$$

If the Heisenberg model is used for $\widetilde{T}$ and $\widetilde{T}_\phi$ (Equations B6 and C6), their ratio reads

$$\frac{\widetilde{T}_\phi}{\widetilde{T}} = C_0 C_{ww}^{-1}\frac{\left[\frac{2}{4} - \frac{1}{4}\frac{k}{k_p}\right]}{\left[\frac{2}{3}\frac{k}{k_p} - \frac{1}{4}\left(\frac{k}{k_p}\right)^2\right]}. \tag{C16}$$

Equation C14 reduces to Equation 9 when rapid-distortion terms are dropped ($\alpha_P = \beta_B = 0$) and when, in the evaluation of $\widetilde{\mathscr{A}}_1$ and $\widetilde{\mathscr{A}}_2$, the Heisenberg (1948) and Katul et al. (2013) models are used for the nonlinear transfer term and the Rotta time scale, respectively, which yields

$$\tilde{A}_1\left(\frac{k}{k_p}\right) = \frac{2}{7} C_H^{-1} C_0^{-1/2} C_{ww}^{-1} \left[\frac{2}{3}\frac{k}{k_p} - \frac{1}{4}\left(\frac{k}{k_p}\right)^2\right]^{-1}$$

$$\tilde{A}_2\left(\frac{k}{k_p}\right) = 2C_H C_0^{-1/2} C_{ww} \left[\frac{2}{3}\frac{k}{k_p} - \frac{1}{4}\left(\frac{k}{k_p}\right)^2\right]\left(\frac{k}{k_p}\right)^{1/3}.$$

(C17)

References

Abid, R., & Speziale, C. G. (1993). Predicting equilibrium states with Reynolds stress closures in channel flow and homogeneous shear flow. *Physics of Fluids A: Fluid Dynamics*, *5*(7), 1776–1782. https://doi.org/10.1063/1.858852

Banerjee, T., & Katul, G. G. (2013). Logarithmic scaling in the longitudinal velocity variance explained by a spectral budget. *Physics of Fluids*, *25*(12), 125106. https://doi.org/10.1063/1.4837876

Banerjee, T., Katul, G. G., Salesky, S. T., & Chamecki, M. (2015). Revisiting the formulations for the longitudinal velocity variance in the unstable atmospheric surface layer. *Quarterly Journal of the Royal Meteorological Society*, *141*(690), 1699–1711. https://doi.org/10.1002/qj.2472

Besnard, D. C., Harlow, F. H., Rauenzahn, R. M., & Zemach, C. (1996). Spectral transport model for turbulence. *Theoretical and Computational Fluid Dynamics*, *8*(1), 1–35. https://doi.org/10.1007/BF00312400

Bos, W. J. T., Touil, H., Shao, L., & Bertoglio, J.-P. (2004). On the behavior of the velocity-scalar cross correlation spectrum in the inertial range. *Physics of Fluids*, *16*(10), 3818–3823. https://doi.org/10.1063/1.1779229

Bou-Zeid, E., Gao, X., Ansorge, C., & Katul, G. G. (2018). On the role of return to isotropy in wall-bounded turbulent flows with buoyancy. *Journal of Fluid Mechanics*, *856*, 61–78. https://doi.org/10.1017/jfm.2018.693

Brugger, P., Katul, G. G., DeRoo, F., Kröniger, K., Rotenberg, E., Rohatyn, S., & Mauder, M. (2018). Scalewise invariant analysis of the anisotropic Reynolds stress tensor for atmospheric surface layer and canopy sublayer turbulent flows. *Physical Review Fluids*, *3*(5), 054608. https://doi.org/10.1103/PhysRevFluids.3.054608

Canuto, V. M., Howard, A., Cheng, Y., & Dubovikov, M. S. (2001). Ocean turbulence. Part I: One-point closure model-momentum and heat vertical diffusivities. *Journal of Physical Oceanography*, *31*(6), 1413–1426. https://doi.org/10.1175/1520-0485(2001)031<1413:OTPIOP>2.0.CO;2

Carbone, M., & Bragg, A. D. (2020). Is vortex stretching the main cause of the turbulent energy cascade? *Journal of Fluid Mechanics*, *883*, R2. https://doi.org/10.1017/jfm.2019.923

Cava, D., Giostra, U., & Tagliazucca, M. (2001). Spectral maxima in a perturbed stable boundary layer. *Boundary-Layer Meteorology*, *100*(3), 421–437. https://doi.org/10.1023/A:1019219117439

Charuchittipan, D., & Wilson, J. D. (2009). Turbulent kinetic energy dissipation in the surface layer. *Boundary-Layer Meteorology*, *132*(2), 193–204. https://doi.org/10.1007/s10546-009-9399-x

Cuxart, J., Bougeault, P., & Redelsperger, J.-L. (2000). A turbulence scheme allowing for mesoscale and large-eddy simulations. *Quarterly Journal of the Royal Meteorological Society*, *126*, 1–30. https://doi.org/10.1002/qj.49712656202

Drobinski, P., Carlotti, P., Redelsperger, J.-L., Masson, V., Banta, R. M., & Newsom, R. K. (2007). Numerical and experimental investigation of the neutral atmospheric surface layer. *Journal of the Atmospheric Sciences*, *64*(1), 137–156. https://doi.org/10.1175/JAS3831.1

Foken, T. (2006). 50 years of the Monin-Obukhov similarity theory. *Boundary-Layer Meteorology*, *119*(3), 431–447. https://doi.org/10.1007/s10546-006-9048-6

Fortuniak, K., & Pawlak, W. (2015). Selected spectral characteristics of turbulence over an urbanized area in the centre of Łódź, Poland. *Boundary-Layer Meteorology*, *154*(1), 137–156. https://doi.org/10.1007/s10546-014-9966-7

Freire, L. S., Chamecki, M., Bou-Zeid, E., & Dias, N. L. (2019). Critical flux Richardson number for Kolmogorov turbulence enabled by TKE transport. *Quarterly Journal of the Royal Meteorological Society*, *145*, 1551–1558. https://doi.org/10.1002/qj.3511

Ghannam, K., Duman, T., Salesky, S. T., Chamecki, M., & Katul, G. (2017). The non-local character of turbulence asymmetry in the convective atmospheric boundary layer. *Quarterly Journal of the Royal Meteorological Society*, *143*(702), 494–507. https://doi.org/10.1002/qj.2937

Ghannam, K., Katul, G. G., Bou-Zeid, E., Gerken, T., & Chamecki, M. (2018). Scaling and similarity of the anisotropic coherent eddies in near-surface atmospheric turbulence. *Journal of the Atmospheric Sciences*, *75*(3), 943–964. https://doi.org/10.1175/JAS-D-17-0246.1

Grachev, A. A., Andreas, E. L., Fairall, C. W., Guest, P. S., & Persson, P. G. (2013). The critical Richardson number and limits of applicability of local similarity theory in the stable boundary layer. *Boundary-Layer Meteorology*, *147*(1), 51–82. https://doi.org/10.1007/s10546-012-9771-0

Heisenberg, W. (1948). On the theory of statistical and isotropic turbulence. *Proceedings of the Royal Society of London. Series A. Mathematical and Physical Sciences*, *195*(1042), 402–406. https://doi.org/10.1098/rspa.1948.0127

Højstrup, J. (1982). Velocity spectra in the unstable planetary boundary layer. *Journal of the Atmospheric Sciences*, *39*(10), 2239–2248.

Kader, B. A., & Yaglom, A. M. (1990). Mean fields and fluctuation moments in unstably stratified turbulent boundary layers. *Journal of Fluid Mechanics*, *212*, 637–662. https://doi.org/10.1017/S0022112090002129

Kader, B. A., & Yaglom, A. M. (1991). Spectra and correlation functions of surface layer atmospheric turbulence in unstable thermal stratification. *Turbulence and Coherent Structures* (pp. 387–412): Springer. https://doi.org/10.1007/978-94-015-7904-9_24

Kaimal, J. C. (1978). Horizontal velocity spectra in an unstable surface layer. *Journal of the Atmospheric Sciences*, *35*(1), 18–24. https://doi.org/10.1175/1520-0469(1978)035<0018:HVSIAU>2.0.CO;2

Kaimal, J. C., & Finnigan, J. J. (1994). *Atmospheric boundary layer flows: Their structure and measurement*: Oxford University Press.

Kaimal, J. C., Wyngaard, J., Izumi, Y., & Coté, O. R. (1972). Spectral characteristics of surface-layer turbulence. *Quarterly Journal of the Royal Meteorological Society*, *98*(417), 563–589. https://doi.org/10.1002/qj.49709841707

Katul, G., & Chu, C.-R. (1998). A theoretical and experimental investigation of energy-containing scales in the dynamic sublayer of boundary-layer flows. *Boundary-Layer Meteorology*, *86*(2), 279–312. https://doi.org/10.1023/A:1000657014845

Katul, G., Hsieh, C.-I., Bowling, D., Clark, K., Shurpali, N., Turnipseed, A., et al. (1999). Spatial variability of turbulent fluxes in the roughness sublayer of an even-aged pine forest. *Boundary-Layer Meteorology*, *93*(1), 1–28. https://doi.org/10.1023/A:1002079602069

Katul, G., Hsieh, C.-I., Kuhn, G., Ellsworth, D., & Nie, D. (1997). Turbulent eddy motion at the forest-atmosphere interface. *Journal of Geophysical Research*, *102*(D12), 13,409–13,421. https://doi.org/10.1029/97JD00777

Katul, G., Hsieh, C.-I., & Sigmon, J. (1997). Energy-inertial scale interactions for velocity and temperature in the unstable atmospheric surface layer. *Boundary-Layer Meteorology*, *82*(1), 49–80. https://doi.org/10.1023/A:1000178707511

Katul, G. G., Konings, A. G., & Porporato, A. (2011). Mean velocity profile in a sheared and thermally stratified atmospheric boundary layer. *Physical Review Letters*, *107*(26), 268,502. https://doi.org/10.1103/PhysRevLett.107.268502

Katul, G. G., Porporato, A., Manes, C., & Meneveau, C. (2013). Co-spectrum and mean velocity in turbulent boundary layers. *Physics of Fluids*, *25*(9), 091702. https://doi.org/10.1063/1.4821997

Katul, G. G., Porporato, A., & Nikora, V. (2012). Existence of k^{-1} power-law scaling in the equilibrium regions of wall-bounded turbulence explained by Heisenberg's eddy viscosity. *Physical Review E*, *86*(6), 066311. https://doi.org/10.1103/PhysRevE.86.066311

Katul, G. G., Porporato, A., Shah, S., & Bou-Zeid, E. (2014). Two phenomenological constants explain similarity laws in stably stratified turbulence. *Physical Review E*, *89*(2), 023007. https://doi.org/10.1103/PhysRevE.89.023007

Kolmogorov, A. N. (1941). The local structure of turbulence in incompressible viscous fluid for very large Reynolds numbers. *Cr Acad. Sci. URSS*, *30*, 301–305.

Lane, T. P., & Sharman, R. D. (2014). Intensity of thunderstorm-generated turbulence revealed by large-eddy simulation. *Geophysical Research Letters*, *41*, 2221–2227. https://doi.org/10.1002/2014GL059299

Launder, B. E., Reece, G. J., & Rodi, W. (1975). Progress in the development of a Reynolds-stress turbulence closure. *Journal of Fluid Mechanics*, *68*(3), 537–566.

Leith, C. E. (1967). Diffusion approximation to inertial energy transfer in isotropic turbulence. *The Physics of Fluids*, *10*(7), 1409–1416. https://doi.org/10.1063/1.1762300

Li, D., Katul, G. G., & Bou-Zeid, E. (2015). Turbulent energy spectra and cospectra of momentum and heat fluxes in the stable atmospheric surface layer. *Boundary-Layer Meteorology*, *157*(1), 1–21. https://doi.org/10.1007/s10546-015-0048-2

Li, D., Katul, G. G., & Zilitinkevich, S. S. (2015). Revisiting the turbulent Prandtl number in an idealized atmospheric surface layer. *Journal of the Atmospheric Sciences*, *72*(6), 2394–2410. https://doi.org/10.1175/JAS-D-14-0335.1

Lovejoy, S., Tuck, A. F., Hovde, S. J., & Schertzer, D. (2007). Is isotropic turbulence relevant in the atmosphere? *Geophysical Research Letters*, *34*, L15802. https://doi.org/10.1029/2007GL029359

Lumley, J. L., & Khajeh-Nouri, B. (1975). Computational modeling of turbulent transport. *Advances in Geophysics*(Vol. 18, pp. 169–192): Elsevier. https://doi.org/10.1016/S0065-2687(08)60460-4

Lumley, J. L., & Newman, G. R. (1977). The return to isotropy of homogeneous turbulence. *Journal of Fluid Mechanics*, *82*(1), 161–178. https://doi.org/10.1017/S0022112077000585

Marusic, I., McKeon, B. J., Monkewitz, P. A., Nagib, H. M., Smits, A. J., & Sreenivasan, K. R. (2010). Wall-bounded turbulent flows at high Reynolds numbers: Recent advances and key issues. *Physics of Fluids*, *22*(6), 065103. https://doi.org/10.1063/1.3453711

McColl, K. A., Katul, G. G., Gentine, P., & Entekhabi, D. (2016). Mean-velocity profile of smooth channel flow explained by a cospectral budget model with wall-blockage. *Physics of Fluids*, *28*(3), 035107. https://doi.org/10.1063/1.4943599

Mellor, G. L., & Yamada, T. (1982). Development of a turbulence closure model for geophysical fluid problems. *Reviews of Geophysics*, *20*(4), 851–875.

Monin, A., & Obukhov, A. (1954). Basic laws of turbulent mixing in the surface layer of the atmosphere. *Geophysical Center of the Russian Academy of Sciences*, *151*(163), e187.

Morrison, J. F., Jiang, W., McKeon, B. J., & Smits, A. J. (2002). Reynolds number dependence of streamwise velocity spectra in turbulent pipe flow. *Physical Review Letters*, *88*(21), 214501. https://doi.org/10.1103/PhysRevLett.88.214501

Nickels, T. B., Marusic, I., Hafez, S., & Chong, M. S. (2005). Evidence of the k_1^{-1} law in a high-Reynolds-number turbulent boundary layer. *Physical Review Letters*, *95*(7), 074501.

Nikora, V. (1999). Origin of the "−1" spectral law in wall-bounded turbulence. *Physical Review Letters*, *83*(4), 734. https://doi.org/10.1103/PhysRevLett.83.734

Obukhov, A. M. (1941). On the spectral distribution of energy in turbulent flow. *Izv. Acad. Sci. U.S.S.R., Geogr. a,d Geophys. Ser.*, *4*(5).

Panchev, S. (1971). *Random functions and turbulence* (Vol. 32). Elsevier.

Poggi, D., Katul, G. G., & Albertson, J. D. (2004). Momentum transfer and turbulent kinetic energy budgets within a dense model canopy. *Boundary-Layer Meteorology*, *111*(3), 589–614. https://doi.org/10.1023/B:BOUN.0000016502.52590.af

Pope, S. B. (2000). *Turbulent flows*: Cambridge University Press. https://doi.org/10.1017/CBO9780511840531

Raupach, M. R. (1981). Conditional statistics of Reynolds stress in rough-wall and smooth-wall turbulent boundary layers. *Journal of Fluid Mechanics*, *108*, 363–382. https://doi.org/10.1017/S0022112081002164

Rotta, J. C. (1951). Statistische theorie nichthomogener turbulenz. *Zeitschrift für Physik*, *129*(6), 547–572.

Saddoughi, S. G., & Veeravalli, S. V. (1994). Local isotropy in turbulent boundary layers at high Reynolds number. *Journal of Fluid Mechanics*, *268*, 333–372. https://doi.org/10.1017/S0022112094001370

Salesky, S. T., Katul, G. G., & Chamecki, M. (2013). Buoyancy effects on the integral lengthscales and mean velocity profile in atmospheric surface layer flows. *Physics of Fluids*, *25*(10), 105101. https://doi.org/10.1063/1.4823747

Schumann, U. (1994). On relations between constants in homogeneous turbulence models and Heisenberg's spectral model. *Beiträge zur Physik der Atmosphäre*, *2*, 141–147.

Sorbjan, Z. (1989). *Structure of the atmospheric boundary layer*. Englewood Cliffs, NJ: Prentice Hall.

Tchen, C. M. (1953). On the spectrum of energy in turbulent shear flow. https://doi.org/10.6028/jres.050.009

Tchen, C. M. (1954). Transport processes as foundations of the Heisenberg and Obukhoff theories of turbulence. *Physical Review*, *93*(4). https://doi.org/10.1103/PhysRev.93.4

Wyngaard, J. C., & Coté, O. R. (1971). The budgets of turbulent kinetic energy and temperature variance in the atmospheric surface layer. *Journal of the Atmospheric Sciences*, *28*(2), 190–201. https://doi.org/10.1175/1520-0469(1971)028<0190:TBOTKE>2.0.CO;2

Zeman, O., & Tennekes, H. (1975). A self-contained model for the pressure terms in the turbulent stress equations of the neutral atmospheric boundary layer. *Journal of the Atmospheric Sciences*, *32*(9), 1808–1813. https://doi.org/10.1175/1520-0469(1975)032<1808:ASCMFT>2.0.CO;2